Archival Report

Biological Psychiatry: GOS

11.7T Diffusion Magnetic Resonance Imaging and Tractography to Probe Human Brain Organoid Microstructure

Amelia Versace, T. Kevin Hitchens, Callen T. Wallace, Simon C. Watkins, and Leonardo D'Aiuto

ABSTRACT

BACKGROUND: Human brain organoids are 3-dimensional cellular models that mimic architectural features of a developing brain. Generated from human induced pluripotent stem cells, these organoids offer an unparalleled physiologically relevant in vitro system for disease modeling and drug screening. In the current study, we sought to establish a foundation for a magnetic resonance imaging (MRI)–based, label-free imaging system that offers high-resolution capabilities for deep tissue imaging of whole organoids.

METHODS: An 11.7T Bruker/89 mm microimaging system was used to collect high-resolution multishell 3-dimensional diffusion images of 2 induced pluripotent stem cell–derived human hippocampal brain organoids. The MRI features identified in the study were interpreted on the basis of similarities with immunofluorescence microscopy.

RESULTS: MRI microscopy at ≤40 μm isotropic resolution provided a 3-dimensional view of organoid microstructure. T2-weighted contrast showed a rosette-like internal structure and a protruding spherical structure that correlated with immunofluorescence staining for the choroid plexus. Diffusion tractography methods can be used to model tissue microstructural features and possibly map neuronal organization. This approach complements traditional immunohistochemistry imaging methods without the need for tissue clearing.

CONCLUSIONS: This proof-of-concept study shows, for the first time, the application of high-resolution diffusion MRI microscopy to image 2-mm diameter spherical human brain organoids. Application of ultrahigh-field MRI and diffusion tractography is a powerful modality for whole organoid imaging and has the potential to make a significant impact for probing microstructural changes in brain organoids used to model psychiatric disorders, neurodegenerative diseases, and viral infections of the human brain, as well as for assessing neurotoxicity in drug screening.

https://doi.org/10.1016/j.bpsgos.2024.100344

The introduction of human induced pluripotent stem cell (hiPSC)–based technologies has sparked a revolutionary shift in methodological approaches for disease modeling. hiPSCs have presented unparalleled opportunities to generate patient-specific, physiologically relevant 3-dimensional (3D) cultures, known as organoids. These organoids mimic architectural features of developing organs, and brain organoids have increasingly gained popularity for modeling psychiatric disorders, neurodegenerative diseases, and infection of the human brain by neurotropic pathogens (1–4).

The complexity of brain organoids has been accompanied by challenges in achieving high-resolution imaging for these 3D culture systems. Several 3D imaging techniques have been developed that incorporate optical clearing methods to enable the analysis of whole organoids (5). However, the clearing methods, which are aimed at turning tissues transparent to enhance optical imaging depth, may take several days and can lead to organoid deformation and a reduction in fluorescent signals. Thus, there is a need to develop comprehensive 3D imaging methods specifically tailored for large brain organoids, thereby enabling comprehensive analysis of their characteristics and complexity.

Magnetic resonance imaging (MRI) is the standard for clinical imaging of soft tissues. T1-weighted and T2-weighted (T2-w) imaging are useful for delineating brain structures and diagnosing various pathologies. Diffusion-weighted imaging is used to quantify the displacement of water molecules in the brain, which allows for the characterization of the isotropic/anisotropic nature of each voxel. This can be used to estimate the density and microscopic composition of different tissues for healthy and pathological conditions, as well as to map the structural connectivity of the entire brain (6). Thus, while MRI techniques would be useful to probe the 3D anatomy of brain organoids, the small and delicate nature of these structures poses challenges for the use of these techniques.

To date, only 1 study has used MRI to study brain organoids. The approach used 9.4T MRI for serial assessment of groups of brain organoids for monitoring and quality assessment (7). Although the image contrast was relatively modest, a neural network–based computational approach was used to

ISSN: 2667-1743

extract organoid volume and structural features, enabling the identification and segmentation of cystic formations, which are an undesired outcome of brain organoid differentiation (8,9). This novel approach shed light on the potential of high-field MRI as a noninvasive method for investigating the complex structure of brain organoids.

In the current study, we aimed to use ultra-high-field MR microscopy for a more in-depth analysis of brain organoid structural organization. To this end, we used an 11.7T microimaging scanner and a multishell diffusion imaging sequence, which are suitable for the study of microstructural properties of both gray and white matter brain tissues, including diffusion tractography. We anticipated that optimized high-resolution imaging would lead to improved characterization of fine microstructures and cellular organization because it can provide a more comprehensive and detailed understanding of the micro- and mesostructure of the organoids, thereby offering insights into the development and organization of neural networks within these organoids and the effects of disease conditions and treatments. This study utilized hippocampal organoids. The hippocampus, a brain region known for its preserved neurogenetic properties even in adulthood, plays a crucial role in learning and memory. Alzheimer's disease is often associated with hippocampal atrophy, and MRI analysis of hippocampal volume has been used extensively to monitor the progression of this disorder (10–12). Understanding how newly generated hippocampal neurons form connections holds promise for future research in modeling neurodegenerative disorders.

METHODS AND MATERIALS

Generation of Human Brain Organoids

hiPSC line R139361417 (Rutgers University Cell and DNA Repository Infinite Biologics) was used to generate monolayer neuronal cultures and organoids. The hiPSC line was established at the National Institute of Mental Health Center for Collaborative Studies of Mental Disorders–funded Rutgers University Cell and DNA Repository (https://www.coredinates.org). The control steps included analysis of pluripotency markers NANOG, Oct4, TRA60, TRA811, OSX2, and SSEA4. We subsequently conducted karyotyping, array comparative genomic hybridization assays, and short tandem repeat profiling and compared them with donor genomic DNA to evaluate structural changes in genomic DNA during the generation of iPSCs.

The methods used to generate monolayer neuronal cultures and organoids exhibiting features of hippocampal cells are detailed in the Supplement.

Immunofluorescence

Monolayer neuronal cultures were fixed with 4% paraformaldehyde (PFA) and permeabilized with 0.2% Triton-X before immunostaining.

The preparation of frozen sections from organoids was conducted as follows. The organoids were rinsed in phosphate-buffered saline (PBS) and fixed by immersing them in at least 10 volumes of 4% PFA overnight at 4 °C. After 3 washes with PBS, organoids were immersed in 30% sucrose solution overnight. Organoids were gently transferred into cryomolds (Tissue-Tek Cryo Mold Intermediate) followed by the removal of any residual sucrose. Subsequently, the organoids were frozen and embedded into OCT medium at −22 °C. Then, 10-μm sections were prepared by cryostat (Micron HM350; Thermo Fisher Scientific). Frozen sections were stored at −80 °C until needed. Before staining, frozen sections were fixed with 4% PFA for 20 minutes and incubated with 10% goat serum (#50062Z; Thermo Fisher Scientific)/0.2% Triton-X 100 (#X-100; Millipore Sigma) for 1 hour at room temperature.

Samples were incubated with primary antibodies overnight at 4 °C. The primary antibodies used were mouse monoclonal anti-β-tubulin III antibody (1:200 dilution, conjugated clone TUJ1; R and D Systems), rabbit polyclonal anti-FOXG1 antibody (1:1000 dilution; Abcam), rabbit polyclonal anti-GABA antibody (1:500 dilution; Sigma-Aldrich), rabbit polyclonal anti-MAP2 antibody (1:500 dilution; EMD Millipore), mouse monoclonal anti-TTR antibody (1:200 dilution; LSBio), rat monoclonal anti-CTIP2 antibody (1:500 dilution; Abcam), rabbit polyclonal anti-TBR1 antibody (1:500 dilution; Abcam), rabbit polyclonal anti-PROX1 antibody (1:200 dilution; Proteintech) and rabbit polyclonal anti-GRIK4 antibody (ThermoFisher, 1:200 dilution). The following fluorophore-conjugated secondary antibodies were used to detect bound primary antibodies: Alexa Fluor 488 goat antirabbit secondary antibody (1:300 dilution; Thermo Fisher Scientific), Alexa Fluor 488 goat antimouse secondary antibody (1:300 dilution; Thermo Fisher Scientific), Alexa Fluor 594 goat antirabbit secondary antibody (1:300 dilution; Thermo Fisher Scientific), and Alexa Fluor 594 goat antimouse secondary antibody (1:300 dilution; Thermo Fisher Scientific). A fluorescent microscope (Leica CTR5500) and a Nikon A1 point scanning confocal equipped with a 10 × 0.45 numerical aperture objective was used for image acquisition. Nuclei were counterstained with Hoechst 33342.

Whole Organoid Immunostaining

The protocol for this procedure is described in detail in the Supplement.

MRI Procedure and Measurements

MRI was performed at 500 MHz using a Bruker AV3 HD microimaging system equipped with an 11.7T 89-mm vertical-bore superconducting magnet, 16-channel shim insert, micro 2.5 gradient set capable of 1500 mT/m maximum gradient strength, and a 5-mm transverse solenoid radiofrequency coil (Bruker Biospin). Five organoids were used in this study. Securing the organoid in the center of the radiofrequency coil without deforming its delicate structure was a challenge. A sample holder was made from a 5 mm glass NMR tube cut down to approximately 25 mm. A small piece of polyethylene tubing (PE-320) was cut to snugly fit orthogonally in a 5-mm tube. One organoid was deformed while trying to stabilize the position between pieces of gauze. Two organoids were damaged during development of the sample holder. Two organoids were successfully positioned and centered in the polyethylene tubing with PBS solution. To reduce the tissue T1 and facilitate rapid image acquisition, PFA-fixed organoids were soaked in PBS containing 0.2% Gadavist (Bayer

HealthCare) for at least 48 hours prior to high-resolution imaging. The significantly shortened T1 allows for rapid 3D imaging acquisition (short sequence repetition time [TR]), which helps facilitate multishell diffusion experiments with high angularity. The PBS was then replaced with Fluorinert FC-40 (#F9755; Sigma-Aldrich) for magnetic susceptibility matching and to provide a 1H-signal-free background. Because the Fluorinert density is 1.8 g/mL, the organoids rise to the top and could be positioned so as to prevent them from moving during an MRI session. The tube was capped to avoid any air bubbles.

The organoid T1 and T2 were measured before and after Gadavist treatment. T1 was measured with a variable TR spin-echo sequence with 6 exponentially spaced recovery periods and fit to a monoexponential recovery. T2 was measured with a multiecho spin-echo sequence with 30 echoes incremented by 7 or 10 ms. The signal decay was fit to a monoexponential. The 2 positioned organoids were imaged with a multishell 3D spin-echo sequence with 27 and 80 diffusion directions, respectively. Stejskal-Tanner diffusion gradients (δ/Δ 4/12ms) were used with isotropic resolution and field of view = 3.6 $\times$ 3.6 $\times$ 3.6 mm^3; TR and echo time were 200 ms and 20 ms, respectively. Sample temperature was maintained at 12 °C. One sample was imaged with a 72 $\times$ 72 $\times$ 72 matrix, which was transformed to 96 $\times$ 96 $\times$ 96 (40-μm isotropic resolution) with 27 diffusion directions with 3 b values (b = 500 s/mm^2, 6 directions; b = 1000, 9 directions; b = 2000, 12 directions) and 3 A0 images, having an acquisition time of 12 hours. A second organoid was imaged with a matrix of 128 $\times$ 128 $\times$ 128 (30-μm isotropic resolution). The multishell scheme had a TR/echo time = 120/20 ms and 80 noncollinear diffusion directions with 4 b values (b = 1000 s/mm^2, 8 directions; b = 2000, 16 directions; b = 3000, 24 directions; b = 6000, 32 directions) and 8 A0 images, with an acquisition time of 35 hours. This would take >15 times longer using a TR equal to the pre-Gd T1.

MRI Data Preprocessing and Analysis

The same analytic pipeline was used for both MRI experiments. This took approximately 3 to 5 hours for each organoid, accounting for the experimental nature of the study. However, implementation of an optimized and semiautomatic pipeline across all experiments would significantly decrease the total processing time. The diffusion imaging toolbox of the FMRIB Software Library (FSL) [(13); https://fsl.fmrib.ox.ac.uk/fsl/fslwiki] and mrtrix-3 (https://www.mrtrix.org) (14) were used for the analysis of the diffusion MRI (dMRI) data. Raw diffusion-weighted images were first denoised using *dwidenoise* (14–17). Motion distortions were reduced using the FSL diffusion imaging toolbox (18). For spin-echo pulse sequences, magnetic field inhomogeneities and susceptibility effects are negligible; therefore, additional corrections were not necessary. Global fiber tracking was also performed with DSI studio (https://dsi-studio.labsolver.org) using generalized q-series difussion imaging reconstruction (19). After minimal preprocessing, volumetric analysis and global and local tractography were performed as described below.

Analysis of Differentiating Rosette-Like Structures

Differentiating rosette-like structures (DRLSs) were manually traced using the mean of the A0 images for each MRI experiment. A comparison of the count and size of the DRLSs was done to assess the ability of high-field MRI to detect microscopic structural properties of brain organoids. This further allowed us to determine the reproducibility and reliability of the differentiation strategies. This is important when modeling psychiatric and neurodevelopmental disorders and brain infections using brain organoids (20–23). For instance, a reduced count and size of DRLSs in differentiating organoids can indicate variations in the proliferation of radial glial cells (24).

Global and Local Tractography

To explore diffusion MR postprocessing, gray matter, white matter, and cerebrospinal fluid (CSF) response functions, typically used in brain analysis, were applied to estimate the fiber orientation distributions within each voxel using *dwi2response* for multishell data (*dhollander* algorithm) (25). This allowed for a label-free, data-driven segmentation of the dMRI data. Subsequently, *tckgen* (14) was used to apply a probabilistic reconstructing algorithm (*iFOD2*) (25). Here, 2 different tractographic approaches (global and local tractography) were used. For global tractography, the whole organoid mask was used as seed region. Assessment of the streamline organization was probed by manipulating the minimum streamline length (1–8 mm) while holding other reconstructing parameters steady (normalized quantitative anisotropy cutoff = 0.14, angular threshold = 70°, and maximum length = 10 mm). Tracking was terminated after 10^6 random seeds to visualize and count the rendered streamlines. For local tractography, 3D masks of 2 DRLSs served as seed and end regions. Streamline count, streamline length, and mean fractional anisotropy (index of anisotropy indirectly reflecting white matter integrity and collinearity in a given voxel) properties were derived for both global and local tractography.

RESULTS

Generation of Human Brain Organoids

We utilized a differentiation strategy by adapting an approach that enables the generation of hippocampal neurons (26). iPSCs were cultured in low attachment 96-well plates to generate embryoid bodies (EBs). EBs were then exposed to anticaudalizing factors DKK1, noggin, and SB431542 for 3 weeks to inhibit the formation of the caudal neural tube and promote the formation of the rostral neural tube, which gives rise to the brain. Furthermore, cyclopamine, an antagonist of the sonic hedgehog pathway, was applied to enrich for dorsal forebrain progenitors. During development, Wnt signaling regulates cell proliferation and fate specification of the dentate gyrus and cornu ammonis fields of the hippocampus (27,28). Thus, to induce hippocampal differentiation, EBs were treated with a differentiation medium containing 20 ng WNT3A, in addition to BDNF (brain-derived neurotrophic factor), ascorbic acid, and cyclic AMP for the 3-week period. This treatment was followed by 6 weeks of differentiation without WNT3A. By employing this differentiation strategy, we achieved the production of a seamless structure comprising choroid plexus and medial pallium tissues. In fact, most of the differentiating

tissues comprised a central body along with a papillary-thin protrusion.

Immunohistochemistry analysis in one organoid, which was randomly chosen from among those demonstrating consistent organizational patterns, showed the expression of the neuronal marker MAP2 (Figure 1A, B) and the telencephalic marker FOXG1 (Figure 1C) in the main body but not in the protrusion. Conversely, the distal portion of the protrusion expressed the choroid plexus marker TTR (29) (Figure 1A, B). The region between the main body of these floating cultures and the choroid plexus was found to be devoid of neurons (Figure 1A). Following 4 months of culturing of these tissues, we discerned the appearance of PROX1- and GRIK4-positive neurons (Figure 1E, F), which denote the presence of granule and pyramidal hippocampal neurons, respectively. Additionally, cells expressing CTIP2 [indicative for neurons detected in the dentate gyrus, CA1, and cortical regions (30)] and TBR1 [a marker for both cortical and hippocampal neurons (22)] were conspicuously identified (Figure 1I, J). GABAergic (gamma-aminobutyric acidergic) interneurons were also detected (Figure 1D). During the differentiation process, a pool of organoids was dissociated at day 71 and seeded on Matrigel-coated plates. After 19 days, immunocytochemistry analysis revealed the presence of cells expressing the hippocampal markers PROX1 and GRIK4 (Figure 1G, H).

Collectively, these results indicate that under our culture conditions, hiPSCs differentiated into central nervous system cells exhibiting features of hippocampal cells.

High-Field MRI

A set of different brain organoids were fixed in PFA and successfully positioned in a 5-mm NMR tube for high-resolution imaging at 11.7T. Replacing the aqueous buffer with Fluorinert yielded images free of background signal (Figure 2A–E). By soaking the organoid in 0.2% Gadavist in PBS, the tissue's T1 was reduced by 95% from 1897 $\pm$ 37 ms to 91.1 $\pm$ 0.6 ms, with only a modest reduction in T2 (from 75.9 $\pm$ 0.6 ms to 31 $\pm$ 0.3 ms), which enabled rapid acquisition of 3D images (Figure S1).

Visual Inspection of T2-w MRI and dMRI Data

Microstructural features of the human brain organoid were readily detected by T2-w MRI. DRLSs were observed with local areas of T2 hypointensity (Figures 2D and 3A). Use of the label-free, data-driven segmenting algorithm (blue-green-red mosaic in Figure 3A) revealed that these areas were characterized by isotropic diffusion (depicted by blue voxels in Figure 3A), possibly reflecting their high cellular density, and closely resembled the distribution of DRLSs within the immune-stained organoid (Figure 1). Encircling these DRLSs, green voxels delineate areas of anisotropic diffusion, likely reflecting the formation of elongations that assemble into collinear tract–like structures (Figure 3A). This hypothesis was further reinforced by a striking similarity with the confocal microscopy readout of the immune-stained organoid, where the distribution of DRLSs defined by the nuclear marker Hoechst (also in blue) and the neuronal processes defined by the neuronal marker TUJ1 (also in green) strongly resembled the isotropic/anisotropic mosaic revealed by the dMRI data (Figure 3B).

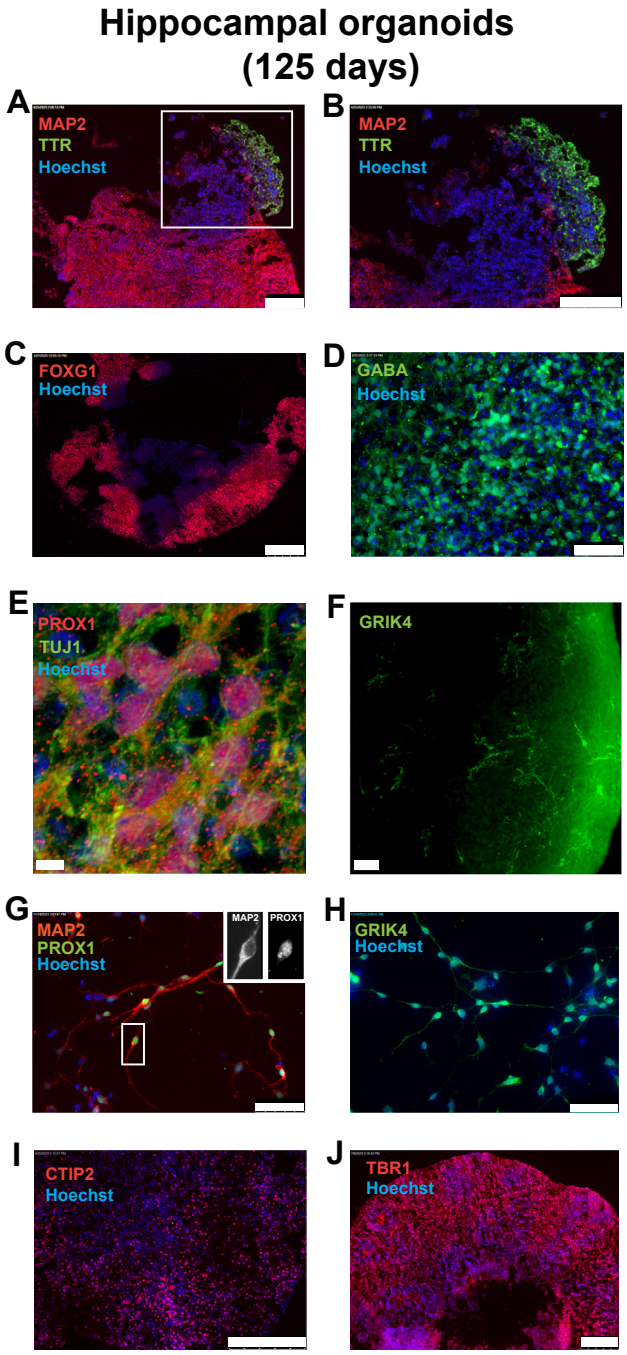

Figure 1. Characterization of 125-day-old brain organoids. **(A–E, I, J)** Immunostaining of 10-μm-thick sections of organoids with antibodies recognizing MAP2/TTR **(A, B)**, FOXG1 **(C)**, GABA **(D)**, PROX1 **(E)**, CTIP2 **(I)**, and TBR1 **(J)**. **(F)** Immunostaining of whole organoid for GRIK4. **(G, H)** Immunostaining of monolayer cultures of neurons generated from differentiating organoids dissociated at day 71 and cultured on Matrigel-coated plate for additional 19 days. Nuclei were counterstained with Hoechst 33342. Scale bar = 250 mm in panels **(A–C, I**, and **J)**, 50 μm in panels **(D, G,** and **H)**, 10 μm in panel **(E),** and 100 μm in panel **(F)**.

A circular structure with varying contrast was also observed at T2-w MRI (Figures 2E and 3A and Figure S2). Its exterior rim had bright T2w image contrast, consistently with mobile water,

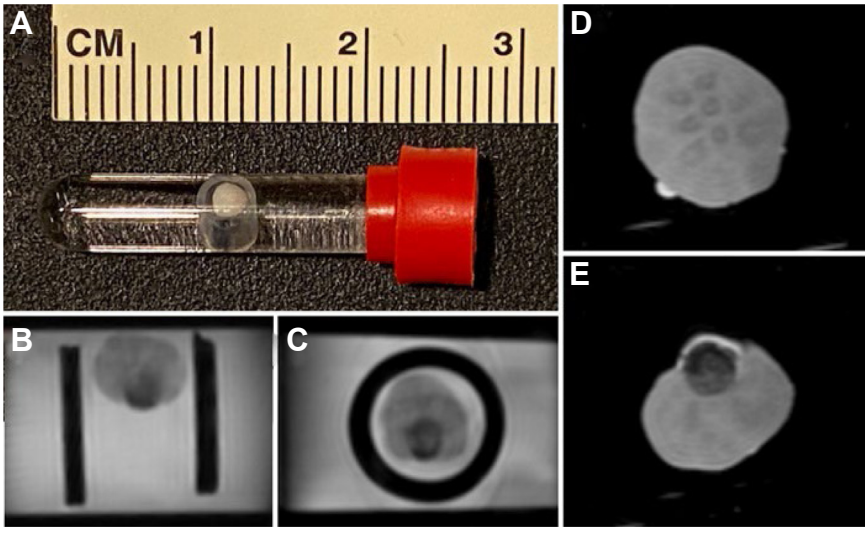

Figure 2. Organoid sample holder for magnetic resonance imaging (MRI). **(A)** Organoid sample holder made from a 5-mm NMR tube and polyethylene (PE) tubing. **(B, C)** Pilot image of an organoid in phosphate-buffered solution (PBS) background. The PE tubing is observed in black contrast with the organoid in the center. **(D, E)** T2-weighted images after replacing PBS with Fluorinert. **(D)** Differentiating rosette-like structures with T2 hypointense contrast in the center of the organoid, with a small residual water droplet visible at the 7-o'clock position. **(E)** A structure presumably containing a choroid plexus and water.

whereas its interior was not well defined (a sequential series of slices from the 40-μm resolution 3D T2-w image is shown in Figure S2). On the dMRI segmentation, the exterior rim was characterized by free water motility, possibly reflecting the presence of CSF, whereas the interior structure was characterized by isotropic diffusion (depicted by red and blue voxels, respectively, in Figure 3A). In the immune-stained organoid, a region with similar characteristics was marked positive for the choroid plexus marker transthyretin (Figure 1A, B).

Volumetric Analysis

The DRLSs of the first organoid (mean [SD] volume = 0.015 [0.005] mm^3) were slightly smaller ($t_7 = -2.4$; $p = .047$) than

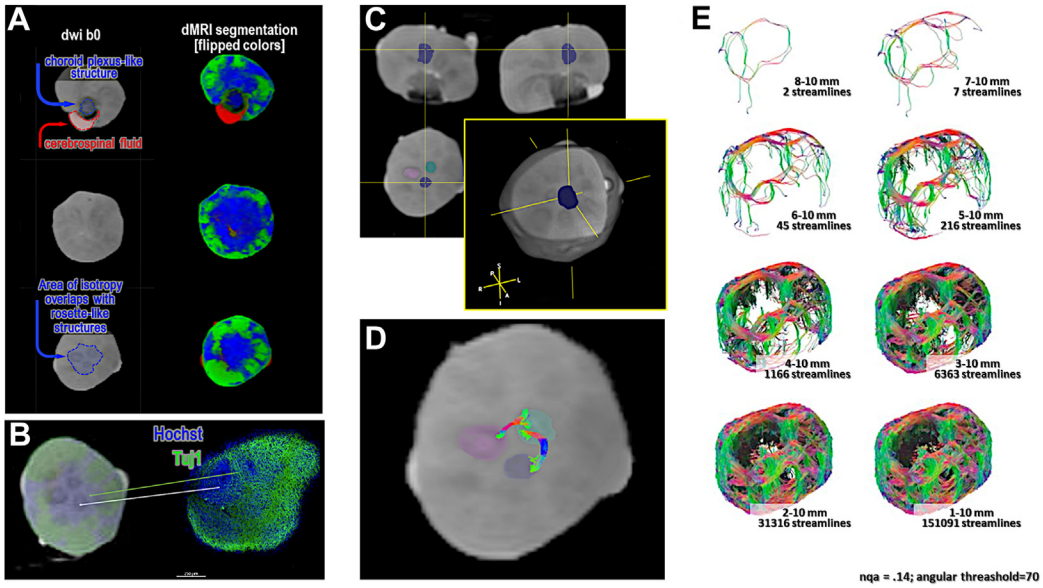

Figure 3. Diffusion magnetic resonance imaging (dMRI) analyses. **(A)** Coronal views of dwi b0 and dMRI segmentation. In dMRI, this segmentation uses a standard color-coding convention, where blue voxels reflect anisotropic areas, and green/red voxels reflect isotropic areas. Here, to enhance the side-by-side comparison with the confocal imaging, the blue/green color coding was switched. **(B)** Side-by-side comparison of the dMRI segmentation and confocal imaging. **(C)** Orthogonal and 3-dimensional (3D) views of one differentiating rosette-like structure superimposed on the mean A0 image. **(D)** Coronal view shown in panel **(C)** is zoomed out to display interconnecting local tractography using color-coding convention in dMRI. **(E)** Reconstruction of whole organoid depicts streamlines using increasing range of streamline length. It is important to acknowledge that streamlines are a visual representation of connecting neighboring voxels with similar orientational diffusion anisotropy, such as voxels in the context of white matter tissue but not only (e.g., muscle tissue), and results are strongly dependent on the setting of main parameters. nqa, normalized quantitative anisotropy.

Table 1. Regions of Interest

Region of Interest	No. Voxels	Volume, mm^3
Organoid 1		
DRLS 1	252	0.013
DRLS 2	438	0.023
DRLS 3	267	0.014
DRLS 4	205	0.011
DRLS 5	291	0.015
Organoid 2		
DRLS 1	1149	0.030
DRLS 2	739	0.019
DRLS 3	675	0.018
DRLS 4	1067	0.028

DRLS, differentiating rosette-like structure.

those of the second organoid (mean [SD] volume = 0.024 [0.006] mm^3) (Table 1 and Figure 3C, D). These findings support the ability of high-field MRI to perform volumetric analysis of DRLSs. Ninety-four percent (i.e., 1367/1453 voxels) of the total volume occupied by the DRLSs overlapped with the blue voxels, and 6% (i.e., 87/1453) overlapped with the green voxels of the segmentation map (Figure S3), indicating that the vast majority of the manually traced DRLSs were characterized by gray matter–like tissue according to the data-driven segmenting algorithm. No voxels (i.e., 0/1453) were characterized by CSF-like tissue (red voxels).

Global and Local Tractography

Streamline reconstruction identified fiber-like organization of the neurons within the organoids. At 30-μm isotropic resolution, an image voxel can contain tens of neurons, and their orientational coherence contribute to water diffusion anisotropy. Global tractography with a default step size value of the IFOD2 (i.e., 0.1) and default tracking parameters (i.e., maximum spherical harmonics degree [lmax] = 8; maximum angular threshold = 45°, random seeds = 10^7) identified fiber-like structures (Table 2) in areas of high anisotropy (i.e., blue voxels in Figure 3A). The use of a 0.01 IFOD2 cutoff revealed the existence of short-range streamlines in the organoid center (Table 2 and Figure 3D), characterized by lower anisotropy and higher cellular density (i.e., green voxels in Figure 3A), possibly reflecting dendritic interconnections (Table 2 and Figure 3D; Supplemental Video). Here, local tractography identified interconnecting fiber-like structures in most—but not all—dyads, suggesting that some DRLSs may be more interconnected than others. Streamline reconstruction (normalized quantitative anisotropy = 0.14, maximum angular threshold = 70°, maximum length = 10 mm, and random seeds = 10^6) reveals features of the overall organization (Figure 3E). Use of progressively decreasing values of the minimal length cutoff revealed that longer streamlines (i.e., 7–10 mm) were located at the perimeter of the circular protrusion. These areas were also associated with higher diffusion anisotropy (not shown). As the streamline cutoff decreases, an increase in the number of rendered streamlines and bundled structures is revealed. The selection of a 1 to 10 mm range enabled the rendering of streamlines throughout the entire organoid, except for the diffusion anisotropy–devoid sphere.

Table 2. Tractography

Seed	Mean (SD)	Minimum	Maximum	Count
Whole Organoid, Step = 0.1	0.4 (0.2)	0.2	2.9	165,785
Whole Organoid, Step = 0.01	0.3 (0.1)	0.2	1.5	116,364
Seed Region, End Region				
DRLS 1, DRLS 2	0.71 (0.42)	0.19	1.17	59
DRLS 1, DRLS 3	1.01 (0.46)	0.40	1.65	118
DRLS 1, DRLS 4	–	–	–	–
DRLS 1, DRLS 5	–	–	–	–
DRLS 2, DRLS 3	0.91 (0.51)	0.20	2.51	104
DRLS 2, DRLS 4	1.65 (0.08)	1.49	2.19	87
DRLS 2, DRLS 5	0.68 (0.04)	0.54	0.74	28
DRLS 3, DRLS 4	2.17 (0.18)	2.03	2.87	18
DRLS 3, DRLS 5	1.63 (1.15)	0.22	3.48	12
DRLS 4, DRLS 5	1.08 (0.06)	0.96	1.20	21

DRLS, differentiating rosette-like structure.

DISCUSSION

Brain organoids, derived from hiPSCs, offer a unique opportunity to study the development and function of the human brain in a controlled laboratory setting. To gain insights into the intricate cellular processes occurring within human brain organoids, researchers depend on sophisticated imaging technologies, such as confocal microscopy, which can be affected by limited penetration depth. We undertook this exploratory MR microscopy study to investigate the feasibility and applicability of high-field and high-resolution MRI to this problem.

While preliminary, our findings suggest that ultra-high-field MRI offers a promising approach for characterizing organoid structure, potentially complementing optical imaging tools. Specifically, ultra-high-field MRI may enable the noninvasive, label-free, and 3D imaging of the entire organoid, thereby providing a whole organoid characterization of its internal structure and organization.

T2-w MRI showed different tissue contrast, revealing the presence of DRLSs and a semispherical protruding structure that is devoid of neuronal markers and positive for the choroid plexus marker TTR compared with confocal microscopy. We speculate that the bright T2-w image contrast and lack of anisotropy could reflect the CSF produced by the choroid plexus–like structure. By combining dMRI with a data-driven segmenting algorithm, we probed microstructural architectures of whole organoids, where areas with high isotropy exhibited similarities to those marked positive for nuclei, whereas those with high anisotropy exhibited similarities to those that marked positive for neuronal markers at confocal microscopy.

Advanced reconstructing algorithms have been extensively utilized with animals and humans to assess complex microstructural features, including dendritic/axonal coherence typical of highly packed fibers; orientation dispersion typical of more complex architectures such as crossing, bending, kissing, fanning fibers; and intraneuritic (e.g., dendritic/axonal

density) and extraneuritic (e.g., CSF, glia) volume fractions. Intriguingly, in organoids, these algorithms revealed discrete streamlines indicative of fiber-like connections. Similarly, changes in diffusion tractography could be used to probe pathology-induced changes to the tissue microstructure and whole organoid connections.

However, when interpreting these findings, it is important to acknowledge that streamlines are a visual representation of connecting neighboring voxels with similar orientational diffusion anisotropy, such as that observed in white matter fiber tracts and bundles. While the brain organoids are composed of nervous tissue by design, diffusion streamlines can also be reconstructed in other structured tissues that are not white matter fiber tracts; examples include the heart, kidney, and muscle (31,32).

There are several limitations of the current study. We acknowledge that our study did not involve MRI alongside immunostaining of the same organoids, which would definitively demonstrate that the streamlines detected by MRI are real and represent structural or functional aspects of the organoids. Our current approach poses limitations in maintaining the 3D coordinates of the organoid throughout the process. We considered different strategies to address this challenge, but to date, we have not found a solution that would limit compromising the structure of the organoid or the quality of the MRI data. In addition, the small number of organoids included in the study limited the use of rigorous statistics. Furthermore, the development of in vivo scanning methods was not possible due to resource limitations. Securing ad hoc funding would enable conducting a large-scale organoid study, facilitating the development of in vivo scanning strategies, optimized protocols to archive MRI and immunostaining of the same organoids, and assembling of semiautomated analytic pipelines to ultimately address current limitations. However, further investigation is necessary to determine the feasibility of repeated measurements without compromising organoid viability.

While further systematic study is needed to validate this approach, the reconstruction of whole organoid streamlines and quantification of changes in terms of streamline length and volume hold great potential for 1) characterizing neuronal differentiation, 2) staging organoid development, and 3) probing the impact of various conditions (e.g., infection) on these processes. This becomes particularly important when evaluating the effect of newly identified hits from drug screening campaigns on neuronal growth. Additional research is warranted to further explore the use of high-field dMRI in characterizing brain organoid structures and the changes associated with models of psychiatric disorders and neurodegenerative diseases (21–24).

Conclusions

The use of ultra-high-field MRI for brain organoids analysis holds significant potential to advance the application of brain organoids for disease modeling purposes. In addition, proving the feasibility and utility of ultra-high-field MRI to the study of human brain organoids can improve the reproducibility and standardization of imaging results across different samples and large-scale research studies. While we recognize the importance of further validating our findings by coregistering MRI with immunostaining techniques, given current technological constraints, we believe that our results still contribute valuable insights to the use of ultra-high-field MRI to characterize brain organoids. By establishing the feasibility of this technique, this study paves the way for future investigations that can leverage advancements in coregistration methodologies. Progress in this direction holds the potential to increase research reliability, establish validity, and knowledge exchange across different fields of research (neural development, cancer, treatment discovery, neurological and psychiatric disorders). Such progress could also be instrumental for drug screening to evaluate the effects of drugs on neurodevelopmental processes and investigate drug neurotoxicity.

ACKNOWLEDGMENTS AND DISCLOSURES

This work was funded by National Institute of Mental Health Grant Nos. 1R01MH114881 and 1R01MH128229 to AV, and National Institute of Neurological Disorders and Stroke Grants Nos. 1R01NS115082-01A1 and 1R21NS096405-01A1 to LD. MRI was performed in the Advanced Imaging Center (RRID:SCR_025139) at the University of Pittsburgh, and the services and instruments used in this project were graciously supported, in part, by the University of Pittsburgh, the office of the Senior Vice Chancellor for Health Sciences, and the Department of Neurobiology.

We thank Lesley M. Foley for technical assistance with preparing samples for MRI.

The authors report no biomedical financial interests or potential conflicts of interest.

ARTICLE INFORMATION

From the University of Pittsburgh Department of Psychiatry, Pittsburgh, Pennsylvania (AV, LD); University of Pittsburgh Magnetic Resonance Research Center, Pittsburgh, Pennsylvania (AV); University of Pittsburgh Department of Neurobiology, Pittsburgh, Pennsylvania (TKH); Advanced Imaging Center, University of Pittsburgh, Pittsburgh, Pennsylvania (TKH); and University of Pittsburgh Department of Cell Biology, Pittsburgh, Pennsylvania (CTW, SCW).

Address correspondence to Amelia Versace, M.D., at versacea@upmc.edu, or Leonardo D'Aiuto, Ph.D., at daiutol@upmc.edu.

Received Feb 29, 2024; revised May 15, 2024; accepted May 16, 2024.

Supplementary material cited in this article is available online at https://doi.org/10.1016/j.bpsgos.2024.100344.

REFERENCES

1. Dixon TA, Muotri AR (2023): Advancing preclinical models of psychiatric disorders with human brain organoid cultures. Mol Psychiatry 28:83–95.
2. Zhang DY, Song H, Ming GL (2021): Modeling neurological disorders using brain organoids. Semin Cell Dev Biol 111:4–14.
3. Jusop AS, Thanaskody K, Tye GJ, Dass SA, Wan Kamarul Zaman WS, Nordin F (2023): Development of brain organoid technology derived from iPSC for the neurodegenerative disease modelling: A glance through. Front Mol Neurosci 16:1173433.
4. Su X, Yue P, Kong J, Xu X, Zhang Y, Cao W, *et al.* (2021): Human brain organoids as an in vitro model system of viral infectious diseases. Front Immunol 12:792316.
5. Ueda HR, Ertürk A, Chung K, Gradinaru V, Chédotal A, Tomancak P, Keller PJ (2020): Tissue clearing and its applications in neuroscience. Nat Rev Neurosci 21:61–79.
6. Le Bihan D, Iima M (2015): Diffusion magnetic resonance imaging: What water tells us about biological tissues. PLoS Biol 13:e1002203.
7. Deininger L, Jung-Klawitter S, Mikut R, Richter P, Fischer M, Karimian-Jazi K, *et al.* (2023): An AI-based segmentation and analysis pipeline for high-field MR monitoring of cerebral organoids. Sci Rep 13:21231.
8. Lancaster MA, Knoblich JA (2014): Generation of cerebral organoids from human pluripotent stem cells. Nat Protoc 9:2329–2340.

9. Pellegrini L, Bonfio C, Chadwick J, Begum F, Skehel M, Lancaster MA (2020): Human CNS barrier-forming organoids with cerebrospinal fluid production. Science 369:eaaz5626.
10. Yu L, Boyle PA, Dawe RJ, Bennett DA, Arfanakis K, Schneider JA (2020): Contribution of TDP and hippocampal sclerosis to hippocampal volume loss in older-old persons. Neurology 94:e142–e152.
11. Gosche KM, Mortimer JA, Smith CD, Markesbery WR, Snowdon DA (2002): Hippocampal volume as an index of Alzheimer neuropathology: Findings from the Nun Study. Neurology 58:1476–1482.
12. Xu H, Liu Y, Wang L, Zeng X, Xu Y, Wang Z (2023): Role of hippocampal subfields in neurodegenerative disease progression analyzed with a multi-scale attention-based network. NeuroImage Clin 38: 103370.
13. Smith SM, Jenkinson M, Woolrich MW, Beckmann CF, Behrens TEJ, Johansen-Berg H, *et al.* (2004): Advances in functional and structural MR image analysis and implementation as FSL. Neuroimage 23(suppl 1):S208–S219.
14. Tournier JD, Smith R, Raffelt D, Tabbara R, Dhollander T, Pietsch M, *et al.* (2019): MRtrix3: A fast, flexible and open software framework for medical image processing and visualisation. NeuroImage 202:116137.
15. Veraart J, Novikov DS, Christiaens D, Ades-Aron B, Sijbers J, Fieremans E (2016): Denoising of diffusion MRI using random matrix theory. Neuroimage 142:394–406.
16. Veraart J, Fieremans E, Novikov DS (2016): Diffusion MRI noise mapping using random matrix theory. Magn Reson Med 76:1582–1593.
17. Cordero-Grande L, Christiaens D, Hutter J, Price AN, Hajnal JV (2019): Complex diffusion-weighted image estimation via matrix recovery under general noise models. Neuroimage 200:391–404.
18. Andersson JLR, Sotiropoulos SN (2016): An integrated approach to correction for off-resonance effects and subject movement in diffusion MR imaging. Neuroimage 125:1063–1078.
19. Yeh FC, Wedeen VJ, Tseng WYI (2010): Generalized q-sampling imaging. IEEE Trans Med Imaging 29:1626–1635.
20. Esk C, Lindenhofer D, Haendeler S, Wester RA, Pflug F, Schroeder B, *et al.* (2020): A human tissue screen identifies a regulator of ER secretion as a brain-size determinant. Science 370:935–941.
21. Lu X, Yang J, Xiang Y (2022): Modeling human neurodevelopmental diseases with brain organoids. Cell Regen 11:1.
22. Srikanth P, Lagomarsino VN, Muratore CR, Ryu SC, He A, Taylor WM, *et al.* (2018): Shared effects of DISC1 disruption and elevated WNT signaling in human cerebral organoids. Transl Psychiatry 8:77.
23. D'Aiuto L, Caldwell JK, Wallace CT, Grams TR, Wesesky MA, Wood JA, *et al.* (2022): The impaired neurodevelopment of human neural rosettes in HSV-1-infected early brain organoids. Cells 11:3539.
24. Wang L, Li Z, Sievert D, Smith DEC, Mendes MI, Chen DY, *et al.* (2020): Loss of NARS1 impairs progenitor proliferation in cortical brain organoids and leads to microcephaly. Nat Commun 11:4038.
25. Dhollander T, Mito R, Raffelt D, Connelly A (2019): Improved White Matter Response Function Estimation for 3-Tissue Constrained Spherical Deconvolution. Presented at the 27th Annual Meeting of the International Society for Magnetic Resonance in Medicine, Montréal, Québec, Canada.
26. Sarkar A, Mei A, Paquola ACM, Stern S, Bardy C, Klug JR, *et al.* (2018): Efficient generation of CA3 neurons from human pluripotent stem cells enables modeling of hippocampal connectivity in vitro. Cell Stem Cell 22:684–697.e9.
27. Galceran J, Miyashita-Lin EM, Devaney E, Rubenstein JL, Grosschedl R (2000): Hippocampus development and generation of dentate gyrus granule cells is regulated by LEF1. Development 127:469–482.
28. Lee SM, Tole S, Grove E, McMahon AP (2000): A local Wnt-3a signal is required for development of the mammalian hippocampus. Development 127:457–467.
29. Olney KC, Todd KT, Pallegar PN, Jensen TD, Cadiz MP, Gibson KA, *et al.* (2022): Widespread choroid plexus contamination in sampling and profiling of brain tissue. Mol Psychiatry 27:1839–1847.
30. Williams ME, Wilke SA, Daggett A, Davis E, Otto S, Ravi D, *et al.* (2011): Cadherin-9 regulates synapse-specific differentiation in the developing hippocampus. Neuron 71:640–655.
31. Otero HJ, Calle-Toro JS, Maya CL, Darge K, Serai SD (2020): DTI of the kidney in children: Comparison between normal kidneys and those with ureteropelvic junction (UPJ) obstruction. Magma 33:63–71.
32. Khalique Z, Ferreira PF, Scott AD, Nielles-Vallespin S, Firmin DN, Pennell DJ (2020): Diffusion tensor cardiovascular magnetic resonance imaging: A clinical perspective. JACC Cardiovasc Imaging 13:1235–1255.